Applied Geochemistry 66 (2016) 162–173

Contents lists available at ScienceDirect

Applied Geochemistry

journal homepage: www.elsevier.com/locate/apgeochem

Two-dimensional reactive transport modeling of the alteration of a fractured limestone by hyperalkaline solutions at Maqarin (Jordan)

Josep M. Soler

Institute of Environmental Assessment and Water Research (IDAEA-CSIC), Associated Unit: Hydrogeology Group (UPC-CSIC), Jordi Girona 18-26, 08034 Barcelona, Catalonia, Spain

ARTICLE INFO

Article history:
Received 23 July 2015
Received in revised form
18 December 2015
Accepted 20 December 2015
Available online 23 December 2015

Keywords:
Maqarin
Modeling
Fracture
Limestone
Portland cement
Advection
Diffusion
Porosity

ABSTRACT

Two-dimensional reactive transport modeling of the Maqarin Eastern Springs site, a natural analogue for the alteration of a fractured limestone by high-pH Portland cement waters, has been performed using the CrunchFlow code. These 2D calculations included transport by advection–dispersion–diffusion along a single fracture and diffusion in the wall rock. Solute transport was coupled to mineral dissolution and precipitation. A limited sensitivity analysis evaluated the effect of different values of primary mineral surface areas, flow velocity and sulfate concentration of the inflowing high-pH solution.

Major secondary minerals include ettringite–thaumasite, C–S–H/C–A–S–H and calcite. C–S–H/C–A–S–H precipitation is controlled by the dissolution of primary silicates. Ettringite precipitation is controlled by diffusion of sulfate and aluminum from the wall rock to the fracture, with aluminum provided by the dissolution of albite. Calcite precipitation is controlled by diffusion of carbonate from the wall rock. Extents of porosity sealing along the fracture and in the fracture-wall rock interface depend on assumptions regarding flow velocity and composition of the high-pH solution. The multiple episodes of fracture sealing and reactivation evidenced in the fracture infills were not included in the simulations. Results can qualitatively reproduce the reported decrease in porosity in the fractures and in the wall rock next to the fractures. Instances of porosity increase next to fractures caused by carbonate dissolution were not reproduced by the calculations.

1. Introduction

Portland cement is a major component of the engineered barrier system and of structural supports in different concepts for underground repositories for low- and intermediate-level radioactive waste, high-level waste and spent fuel. The interaction between groundwater and cement causes the generation of hyperalkaline solutions (pH 12.5–13.5), which may react with the rocks hosting the repositories and change their physical and chemical properties. Experimental and modeling studies of such interactions have been common in the last years (e.g. Adler, 2001; Read et al., 2001; Savage et al., 2002, 2011; Soler, 2003, 2013; Gaucher et al., 2004; Hoch et al., 2004; Mäder et al., 2005; Soler and Mäder, 2005, 2007, 2010; Sánchez et al., 2006; Marty et al., 2009, 2014; Honty et al., 2010; Soler et al., 2011; Kosakowski and Berner, 2013; Moyce et al., 2014). A common finding of these studies has been a reduction of porosity near the cement–rock interface due to the precipitation of secondary phases. This decrease in porosity would in principle be beneficial for the performance of a repository (decrease in flow and transport properties), with a possible exception when gas is produced by the waste.

A case of particular interest would be the contact between cement and a fractured rock formation where water flows mainly through the fractures. A natural analogue for such a system is located in Maqarin, northern Jordan (Khoury, 1985; Khoury and Salameh, 1985; Khoury et al., 1985, 1992; Alexander et al., 1992; Khoury and Milodowski, 1992; Clark et al., 1992, 1993; Linklater et al., 1996). At Maqarin, a hydrated-Portland-cement-like rock body has developed from the hydration and carbonation of a cement-like high-temperature metamorphic rock formed from spontaneous combustion of clay-bearing organic-rich biomicritic limestone and marl. High-pH waters (pH 12.5) flow from these rocks into fractured limestone at the Eastern Springs site, causing a marked mineralogical alteration in the fractures and in the wall rock next to the fractures.

After initial calculations from Chambers and Haworth (1998) providing valuable insight regarding the expected overall

E-mail address: josep.soler@idaea.csic.es.

http://dx.doi.org/10.1016/j.apgeochem.2015.12.012
0883-2927/

evolution of mineralogy, Steefel and Lichtner (1998) performed two-dimensional reactive transport simulations of the hyperalkaline system at the Eastern Springs site. In their 1D fracture flow model they calculated a fracture aperture and flow velocity from an analytical solution of the reaction front geometry and the observed thicknesses of the alteration halos next to the fractures, giving a fracture aperture of 0.22 mm and a velocity of 341 m/day. Their reactive transport model resulted in a reduction in porosity in the wall rock close to the fracture, due mainly to the precipitation of ettringite, with a smaller contribution from calcium silicate hydrates (C–S–H). The very small buffering of pH along the fracture was due to the very fast flow velocities (ca. 300 m/day) implemented in the fracture. They also raised the issue of sealing of porosity in the fracture vs. sealing of porosity in the wall rock, related to the magnitudes of reaction rates in the 2 domains. Sealing of porosity in the wall rock combined with an open fracture would lead to little buffering of the solutions (no access by diffusion to the wall rock) and propagation of the high-pH plume to long distances. Such a process would be potentially detrimental for the performance of a repository. Sealing of the fracture (as opposed to sealing of the wall rock) required the used of larger reaction rates for secondary minerals in the fracture.

Within the GTS-LCS project (Grimsel Test Site – Long-Term Cement Studies) it was decided to update this modeling study including more recent thermodynamic data regarding cement phases (e.g. calcium silicate hydrates, ettringite) and exploring the issue of porosity sealing in the fracture vs. porosity sealing in the wall rock. Different parallel modeling exercises have been running simultaneously within the project. Results from one-dimensional modeling (diffusion between fracture and rock matrix) have already been published by the UFZ Leipzig/PSI team (Shao et al., 2013). This paper reports on the 2D modeling study (flowing water in fracture plus diffusion in the wall rock) performed at IDAEA-CSIC. In this study, flow rates are based on direct observations at the site, giving flow velocities much smaller than those used by Steefel and Lichtner (1998). A detailed comparison of the different studies will be published once all the exercises and their comparison are completed.

2. Description of the Eastern Springs site at Maqarin

The site is located 16 km north of the city of Irbid and 25 km east of the Jordan River near the village of Maqarin, on the southern bank of the Yarmouk River (border between Syria and Jordan). Adit A6 was constructed in 1979 as part of the site exploration for the then planned Jordan-Syria Unity dam (Pitty and Alexander, 2011). The tunnel originated about 50 m above the river level and was driven southwards along N358° for 450 m horizontally into the hillside. Within the adit, the strata are near horizontal and the level follows essentially the same horizon for 180 m. It is confined within the Bituminous Marl Formation.

This adit offered the potential to examine the effects of the interaction of hyperalkaline groundwater with previously unaltered limestone/marl host rock along a well-defined fracture flowpath, from the point where the groundwater entered fractures in the rock (contact with the cement zone) and at various points along flow paths up to ca. 140 m from the cement zone (Linklater, 1998). Typical fracture zones in the rock (most of them sealed by precipitates) include several parallel to subparallel main fractures, 2–10 cm apart, with openings in the submillimeter to millimeter range, and with a fine anastomosing network of veinlets between them (Smellie, 1998).

Fracture logging in Adit A-6 identified the following types of fracture fills, including several generations of reactivation (Pitty and Alexander, 2011):

- Calcium-silicate hydrates (C–S–H, undifferentiated).
- Early Calcite. It is the earliest mineralization observed in veins (before thermal metamorphism).
- Ettringite/Thaumasite (undifferentiated). This is typically fine cross-fiber vein mineralization.
- Jennite. It was only identified in a limited number of fractures where detailed mineralogical data (petrography, XRD, EPMA) were obtained. Elsewhere, jennite (if present) was logged as C–S–H.
- Tobermorite. Tobermorite veining is locally well-developed. Possibly, some fine tobermorite mineralization has not been recognized and may have been logged as C–S–H.
- Gypsum. Fine white gypsum coatings are distinguishable in some cases.
- Late Calcite (Travertine). Late calcite (or calcium carbonate) precipitates usually accompany features associated with active high-pH groundwater discharge. This is typified by coatings of fine white tufa (travertines). These form the latest mineralization on fracture surfaces.

Zeolites have also been identified as a late-stage mineralization. Regarding wall-rock alteration, it appears to be limited from a few mm up to about 3 cm from the fractures. The most intense alteration is found close to the cement zone, with an overall decrease downstream from this zone (Linklater, 1998). The detailed centimeter to tens-of-micrometers structure of the altered rock shows a very high complexity, changing many times within very small (cm) spatial scales.

Regarding the changes in porosity caused by the alteration, there has been reported evidence of increased porosities in narrow zones (up to a few mm) next to fractures close to the cement zone caused by the dissolution of carbonates, while further away there may be a decrease or no change in porosity (Smellie, 1998; Linklater, 1998; Baker et al., 2002). In a more recent study, Martin et al. (2014) and Martin and Leemann (2014) report a systematic decrease in porosity next to the fractures, from very close to the cement zone to several tens of meters away, due to the precipitation of C–A–S–H. In some cases the pores got tightly filled while in other cases some porosity was preserved. Zeolites precipitated at the far end of the hyperalkaline plume. Their interpretation calls for an earlier stage when Ca–Si–(Al) rich fluids caused the filling of the pores next to the fractures, and a later stage when S-rich solutions caused the precipitation of the ettringite fracture fillings. In prior studies this order was reversed, calling first for ettringite–-thaumasite precipitation in the fractures and a later C–S–H stage with fracture reactivation, dissolution and replacement of earlier ettringite–thaumasite and major wall rock alteration (Linklater, 1998; Smellie, 1998).

3. Description of the reactive transport code

Reactive transport modeling was performed using CrunchFlow (Steefel, 2009; Steefel et al., 2015), which is a software package for multicomponent and multidimensional reactive transport in porous media. Details of the code can be found in the user's manual (downloadable from www.csteefel.com).

CrunchFlow solves numerically the advection-dispersion-reaction equations. Since mineral reactions are described using kinetic rate laws, initial mineral surface areas and several reaction rate parameters have to be supplied by the user as input. In this set of simulations, the reaction rate laws that have been used are of the form

$$R_m = A_m \sum_{terms} k_{25} \left(\prod_i a_i^{n_i} \right) f_m(\Delta G) \quad (1)$$

where R_m is the reaction rate for a given mineral in units of mol/m^3rock/s, A_m is the mineral surface area (m^2/m^3rock), k_{25} is the reaction rate constant (mol/m^2/s) at 25 °C, $a_i^{n_i}$ is the term describing the effect of species i on the rate (e.g. effect of H^+), and $f_m(\Delta G)$ is the function describing the dependence of the rate on solution saturation state. The summation term indicates that several parallel rate laws may be used to describe the dependence of the rate on pH or on other species.

The $f_m(\Delta G)$ function has the form

$$f_m(\Delta G) = [1 - \exp(m_2 g^{m_3})]^{m_1} \quad (2)$$

where

$$g = \frac{\Delta G}{RT} = \ln \frac{IAP}{K_{eq}} \quad (3)$$

and ΔG is the Gibbs energy of the reaction (J/mol), IAP is the ionic activity product of the solution with respect to the mineral and K_{eq} is the equilibrium constant for that mineral reaction (ionic activity product at equilibrium).

Regarding the treatment of solid solutions, a kinetic approach similar to the one proposed by Carey and Lichtner (2006, 2007) and Lichtner and Carey (2006) has been used. Given a binary solid solution with compositional end-members AC and BC, solids with discrete compositions such as BC, $A_{0.1}B_{0.9}C$, $A_{0.2}B_{0.8}C$, …, AC are defined. The dissolution reaction for each of these compositions can be written as

$$A_xB_{1-x}C \Leftrightarrow xA + (1-x)B + C \quad (4)$$

The equilibrium constant for this reaction will be defined as

$$K_{ss}(x_{ss}) = (K_1\lambda_1 x_{ss})^{x_{ss}} (K_2\lambda_2(1-x_{ss}))^{1-x_{ss}} \quad (5)$$

where K_1 and K_2 are the equilibrium constants for the dissolution reactions of end-members AC and BC, respectively, x_{ss} is the mol fraction of AC and λ_1 and λ_2 are the activity coefficients of end-members AC and BC in the solid solution, respectively. Once defined in this manner, the reaction of each discrete composition in a solid solution is treated just as any other phase (Eq. (1)). For the sake of simplicity, only a few intermediate terms in the solid solution series have been taken into account.

4. Model parameters

4.1. Dimensions

Fig. 1 shows the setup of the numerical domain with dimensions. This is a two-dimensional domain including a single fracture (1-mm wide) and wall rock (5-cm wide). This setup would correspond to a spacing of 10 cm between individual fractures in a fracture zone. The length of the domain is 82 m, which corresponds approximately to the estimated flow path distance between the cement zone (M1 site) and the sampling point (seepage, M2 site; Linklater, 1998).

All external boundaries are no-diffusive-flux boundaries ($\partial c/\partial x = 0$ or $\partial c/\partial y = 0$), except where water flows into or out of the domain at the fracture ends. At those points an advective flux condition has been used.

Grid spacing was 1 cm in the first 10 cm of the domain along the direction of the fracture (x) and it increased up to 4 m further away from the inlet. In the direction normal to the fracture (y), spacing increased form 0.25 mm in the fracture and in the first 3 mm of rock up to 5 mm further away from the fracture.

4.2. Composition of rock and fracture

Tables 1 and 2 show the initial composition of rock and fracture in the calculations. Rock composition is based on the composition reported by Smellie (1998) for the unaltered Bituminous Marl Fm. (also called Muwaqqar Fm.), not including the minor amounts of pyrite, apatite and iron oxides. Initial porosity is equal to 30%. Muscovite was used instead of illite because equilibrium with respect to this phase produced a better match to measured porewater composition.

Mineral surface areas were calculated assuming a grain radius equal to 1 μm (micritic texture; reference case). Separate calculations were also performed using surfaces areas for the primary minerals smaller by a factor of 10,000. Initial porosity of the fracture was assumed to be equal to 90%, with the corresponding 10% of solid providing reactive surface area in the fracture. Mineral contents and surface areas were scaled from those in the rock. Separate calculations (not shown) were also performed with initial porosity in the fracture equal to 100%, and the results were not significantly different.

The potential secondary phases taken into account were ettringite–thaumasite solid solution, brucite, portlandite, C–S–H solid solution, zeolites (analcime, laumontite, mesolite, natrolite, scolecite, gismondine, mordenite, wairakite), prehnite (C–A–S–H), crystalline C–S–H phases (foshagite, gyrolite, hillebrandite, okenite, tobermorite-14A), gypsum and saponites (Ca, K, Mg, Na). The use of prehnite as an analogue for calcium aluminum silicate hydrate (C–A–S–H) has been discussed by Soler (2013).

4.3. Solution composition

Initial compositions of the rock porewater and of the inflowing high-pH solution are given in Table 3. They are based on the compositions reported by Smellie (1998) and equilibrated with respect to the phases indicated in Table 3. Total SO_4^{2-} concentration of the high-pH solution was fixed to 8.5e-5 mol/kg_H_2O (reference case) to avoid supersaturation with respect to the ettringite–thaumasite solid solution series. Separate calculations were also performed with the sulfate concentration reported by Smellie (1998; 2.97e-3 mol/kg_H_2O) to check the possible effect of using the different concentration values.

In their modeling, Steefel and Lichtner (1998) assumed a slightly different composition of the boundary high-pH solution, corresponding to a different site about 2 km SE from adit A6.

4.4. Thermodynamic data

Forty two minerals and forty species in solution have been taken into account in the calculations. The selection of minerals is based on the primary and secondary phases observed at the site, together with phases that may show supersaturation in solution after reaction (brucite, saponites). All the chemical equilibria in solution are listed in Table 4. The equilibrium constants for all the mineral reactions are given in Table 5. All the equilibrium constants at 25 °C were taken from the database included in CrunchFlow, which is based on the EQ3/6 database (Wolery et al., 1990), except for the C–S–H and ettringite–thaumasite solid solution series and portlandite. The constants for the C–S–H solid solution phases were calculated from the data in Kulik and Kersten (2001). The constants for the ettringite–thaumasite solid solution phases were calculated

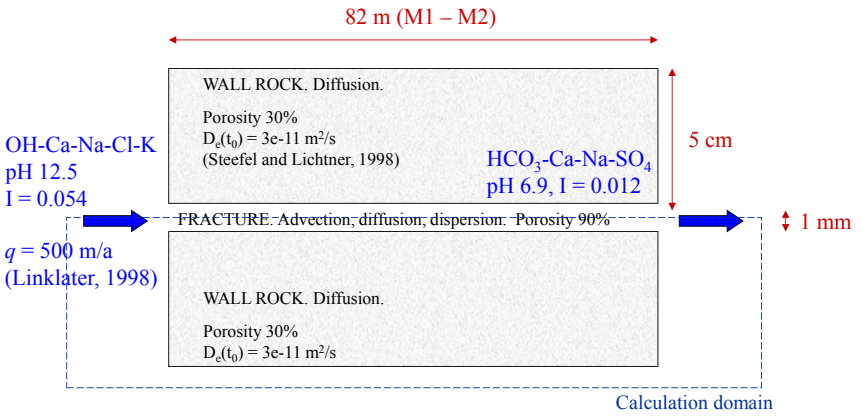

Fig. 1. Schematic representation of the numerical domain, dimensions and reference parameters.

Table 1
Initial composition of the rock (reference case).

Mineral	Vol. frac.	A (m^2/m^3)
Calcite	0.611	1.83e6
Dolomite	0.009	2.58e4
Albite	0.008	2.28e4
Muscovite	0.013	3.87e4
Kaolinite	0.03	9.15e4
Chalcedony	0.029	8.80e4
Porosity	0.3	–

Table 2
Initial composition of the fracture (reference case).

Mineral	Vol. frac.	A (m^2/m^3)
Calcite	0.088	2.62e5
Dolomite	0.001	3.68e3
Albite	0.001	3.26e3
Muscovite	0.002	5.54e3
Kaolinite	0.004	1.31e4
Chalcedony	0.004	1.26e4
Porosity	0.9	–

Table 3
Compositions of the initial solution in rock and fracture and of the inflowing high-pH solution (total molalities, pH and T). Imposed constraints to calculate some of these values (equilibrium with solids or charge balance) are also indicated.

	Rock – fracture	High pH (ref. case)	High pH (high SO_4)
T (°C)	25	25	25
pH	6.92	12.46 charge bal.	12.45 charge bal.
SiO_2	1.85e-4 Chalcedony	7.28e-7 CSH-1667	7.11e-7 CSH-1667
Ca^{2+}	2.97e-3 Calcite	1.98e-2 Portlandite	2.24e-2 Portlandite
Mg^{2+}	1.96e-4 Dolomite	4.71e-9 Brucite	5.69e-9 Brucite
Na^+	2.13e-3	2.05e-3	2.05e-3
K^+	3.18e-4 Muscovite	3.40e-4	3.40e-4
Cl^-	1.79e-3	1.66e-3	1.66e-3
SO_4^{2-}	7.65e-4	8.50e-5	2.97e-3
HCO_3^-	6.70e-3 charge bal.	8.01e-6 Calcite	7.99e-6 Calcite
Al^{3+}	2.22e-9 Kaolinite	8.68e-8 EtTh-Et10	4.00e-9 EtTh-Et10

from the solubilities of end-member ettringite and thaumasite in the CEMDATA07 database (Schmidt et al., 2008) and assuming an ideal solid solution. Although the crystallographic structures of ettringite and thaumasite are not identical, they are similar enough to allow some solid solution between them (Edge and Taylor, 1971; Taylor, 1997). log K_{eq} for portlandite is from Hummel et al. (2002).

Table 4
Equilibrium constants (log K_{eq}) for equilibria in solution. Reactions are written as the destruction of 1 mol of the species in terms of Al^{3+}, $SiO_2(aq)$, Na^+, K^+, Ca^{2+}, Mg^{2+}, HCO_3^-, SO_4^{2-}, H^+, Cl^- and H_2O.

Species	log K_{eq}	Species	log K_{eq}
$Al(OH)_2^+$	1.0594E+01	KOH(aq)	1.4460E+01
AlO_2^-	2.2879E+01	KSO_4^-	−8.7500E-01
$AlOH^{2+}$	4.9564E+00	$Mg_4(OH)_4^{4+}$	3.9750E+01
$CO_2(aq)$	−6.3414E+00	$MgCO_3(aq)$	7.3562E+00
CO_3^{2-}	1.0325E+01	$MgCl^+$	1.3865E-01
$CaCO_3(aq)$	7.0088E+00	$MgHCO_3^+$	−1.0329E+00
$CaCl^+$	7.0039E-01	$MgSO_4(aq)$	−2.4125E+00
$CaCl_2(aq)$	6.5346E-01	$NaAlO_2(aq)$	2.3627E+01
$CaHCO_3^+$	−1.0429E+00	$NaCO_3^-$	9.8156E+00
$CaOH^+$	1.2850E+01	NaCl(aq)	7.8213E-01
$CaSO_4(aq)$	−2.1004E+00	$NaHCO_3(aq)$	1.5573E-01
$H_2SiO_4^{2-}$	2.2960E+01	$NaHSiO_3(aq)$	8.2984E+00
$HAlO_2(aq)$	1.6431E+01	NaOH(aq)	1.4799E+01
$HSiO_3^-$	9.9422E+00	$NaSO_4^-$	−8.2000E-01
KCl(aq)	1.5004E+00	OH^-	1.3991E+01

4.5. Reaction rates

Table 6 shows the rate parameters used for the primary minerals. Regarding the secondary minerals, fast kinetics have been assumed (A_m = 1e6 m^2/m^3, k_m = 1e-8 mol/m^2/s), simulating local equilibrium.

4.6. Flow and transport parameters

Linklater (1998) reports two values of flow rates for 2 individual fractures at the M2 sampling site. Those values are 1.92e-3 are 1.85e-2 L/m^2/s, or equivalently 60.6 and 583.4 m/a. Based on those numbers, a Darcy velocity q equal to 500 m/a was chosen for the flow velocity in the fracture (reference case). A separate calculation with q = 1e5 m/a was also performed to compare with results using a flow velocity similar to the one used by Steefel and Lichtner (1998; 341 m/d = 1.24e5 m/a).

Longitudinal and transverse dispersivity values (1 m and 1e-4 m, respectively) were arbitrarily chosen on the basis of the dimensions of the fracture. Diffusion is the only transport mechanism in the wall rock. The effective diffusion coefficient for all the species in the whole domain is calculated using the expression

$$D_e = \varphi \tau D_0 \quad (6)$$

with D_0 equal to 1e-9 m^2/s. τ is tortuosity, which is kept constant during the calculations. As a result D_e will change linearly with

Table 5
Equilibrium constants (log K_{eq}) for mineral reactions, written as the dissolution of 1 mol of the mineral in terms of Al^{3+}, $SiO_2(aq)$, Na^+, K^+, Ca^{2+}, Mg^{2+}, HCO_3^-, SO_4^{2-}, H^+, Cl^- and H_2O. EtTh and CSH terms refer to discrete compositions in the ettringite–thaumasite and C–S–H solid solution series.

Mineral	Formula	log K_{eq}	Mineral	Formula	log K_{eq}
Calcite	$CaCO_3$	1.8542E+00	CSH-02	$1.16SiO_2{\cdot}0.23Ca(OH)_2{\cdot}0.23H_2O$	1.9648E+00
Dolomite	$CaMg(CO_3)_2$	2.5240E+00	CSH-00	SiO_2	−1.2000E+00
Albite	$NaAlSi_3O_8$	2.7458E+00	Analcime	$Na_{.96}Al_{.96}Si_{2.04}O_6{\cdot}H_2O$	6.1267E+00
Muscovite	$KAl_3Si_3O_{10}(OH)_2$	1.3567E+01	Laumontite	$CaAl_2Si_4O_{12}{\cdot}4H_2O$	1.3642E+01
Kaolinite	$Al_2Si_2O_5(OH)_4$	6.7973E+00	Mesolite	$Na_{.676}Ca_{.657}Al_{1.99}Si_{3.01}O_{10}{\cdot}2.647H_2O$	1.3601E+01
Chalcedony	SiO_2	−3.7344E+00	Natrolite	$Na_2Al_2Si_3O_{10}{\cdot}2H_2O$	1.8502E+01
EtTh-Et10	$Ca_6Al_2(SO_4)_3(OH)_{12}{\cdot}26H_2O$	5.6822E+01	Scolecite	$CaAl_2Si_3O_{10}{\cdot}3H_2O$	1.5859E+01
EtTh-Et08	$Ca_6Al_{1.6}(SiO_3)_{0.4}(SO_4)_{2.8}(OH)_{9.6}(CO_3)_{0.4}{\cdot}26.8H_2O$	4.9063E+01	Gismondine	$Ca_2Al_4Si_4O_{16}{\cdot}9H_2O$	4.1717E+01
EtTh-Et06	$Ca_6Al_{1.2}(SiO_3)_{0.8}(SO_4)_{2.6}(OH)_{7.2}(CO_3)_{0.8}{\cdot}27.6H_2O$	4.1447E+01	Mordenite	$Ca_{.2895}Na_{.361}Al_{.94}Si_{5.06}O_{12}{\cdot}3.468H_2O$	−5.2288E+00
EtTh-Et04	$Ca_6Al_{0.8}(SiO_3)_{1.2}(SO_4)_{2.4}(OH)_{4.8}(CO_3)_{1.2}{\cdot}28.4H_2O$	3.3906E+01	Wairakite	$CaAl_2Si_4O_{10}(OH)_4$	1.8052E+01
EtTh-Et02	$Ca_6Al_{0.4}(SiO_3)_{1.6}(SO_4)_{2.2}(OH)_{2.4}(CO_3)_{1.6}{\cdot}29.2H_2O$	2.6440E+01	Prehnite	$Ca_2Al_2Si_3O_{10}(OH)_2$	3.2914E+01
EtTh-Et00	$Ca_6(SiO_3)_2(SO_4)_2(CO_3)_2{\cdot}30H_2O$	1.9116E+01	Foshagite	$Ca_4Si_3O_9(OH)_2{\cdot}0.5H_2O$	6.5906E+01
Brucite	$Mg(OH)_2$	1.6298E+01	Gyrolite	$Ca_2Si_3O_7(OH)_2{\cdot}1.5H_2O$	2.2893E+01
Portlandite	$Ca(OH)_2$	2.2800E+01	Hillebrandite	$Ca_2SiO_3(OH)_2{\cdot}0.17H_2O$	3.6815E+01
CSH-1667	$SiO_2{\cdot}1.67Ca(OH)_2{\cdot}1H_2O$	2.9133E+01	Okenite	$CaSi_2O_4(OH)_2{\cdot}H_2O$	1.0370E+01
CSH-14	$SiO_2{\cdot}1.4Ca(OH)_2{\cdot}0.95H_2O$	2.3124E+01	Tobermorite	$Ca_5Si_6H_{21}O_{27.5}$	6.3811E+01
CSH-12	$SiO_2{\cdot}1.2Ca(OH)_2{\cdot}0.91H_2O$	1.8801E+01	Gypsum	$CaSO_4{\cdot}2H_2O$	−4.4729E+00
CSH-10	$SiO_2{\cdot}Ca(OH)_2{\cdot}0.86H_2O$	1.4583E+01	Saponite-Ca	$Ca_{.165}Mg_3Al_{.33}Si_{3.67}O_{10}(OH)_2$	2.6268E+01
CSH-08	$2.27SiO_2{\cdot}1.82Ca(OH)_2{\cdot}1.82H_2O$	2.4631E+01	Saponite-K	$K_{.33}Mg_3Al_{.33}Si_{3.67}O_{10}(OH)_2$	2.5986E+01
CSH-06	$1.72SiO_2{\cdot}1.03Ca(OH)_2{\cdot}1.03H_2O$	1.3271E+01	Saponite-Mg	$Mg_{3.165}Al_{.33}Si_{3.67}O_{10}(OH)_2$	2.6230E+01
CSH-04	$1.39SiO_2{\cdot}0.56Ca(OH)_2{\cdot}0.56H_2O$	6.4767E+00	Saponite-Na	$Na_{.33}Mg_3Al_{.33}Si_{3.67}O_{10}(OH)_2$	2.6324E+01

Table 6
Rate parameters for the primary minerals in the rock (see Equation (1)).

Mineral	log k_{25} (mol/m^2/s)	E_a (kcal/mol)	n $(a_{H+})^n$	m_1	m_2	m_3	Refs.
Calcite	−5.81	5.62	0	1	1	1	Palandri and Kharaka, 2004
Calcite	−0.3	3.44	1.0	1	1	1	Same as above
Dolomite	−7.7	11	0	1	1	1	Morse and Arvidson, 2002
Dolomite	−3.1	11	0.63	1	1	1	Same as above
Albite	−10.16	15.5	0.457	14	0.4	1	Palandri and Kharaka, 2004; Burch et al., 1993; Soler and Lasaga, 1996
Albite	−12.56	16.7	0	14	0.4	1	Same as above
Albite	−7.59	17.0	$(a_{OH-})^{0.572}$	14	0.4	1	Same as above
Muscovite	−11.85	13	0.37	1	1	1	Palandri and Kharaka, 2004
Muscovite	−13.55	13	0	1	1	1	Same as above
Muscovite	−14.55	13	−0.22	1	1	1	Same as above
Kaolinite	−11.31	16	0.777	1	1	1	Palandri and Kharaka, 2004
Kaolinite	−13.18	16	0	1	1	1	Same as above
Kaolinite	−17.05	16	−0.472	1	1	1	Same as above
Chalcedony	−11.4	18	0.30	1	1	1	Bandstra et al., 2008 (quartz)
Chalcedony	−14.9	18	−0.40	1	1	1	Same as above

porosity (φ). Initial diffusion coefficients are given in Table 7. Along the fracture diffusion is negligible compared to dispersion.

5. Results

5.1. Reference case and case with small surface areas

Fig. 2 shows the evolution of solution composition (breakthrough) at the fracture outlet, which would correspond to the solution composition at the M2 sampling site. Measured solution composition at the M2 site is almost identical to the inflowing high-pH solution (M1 and M2 sites, Smellie, 1998). That would not be the case for any of the 2 cases shown in Fig. 2. pH at outlet (11.1) becomes more similar to the measured value (12.5) in the case with small surface areas, but still the solution shows important changes with respect to the inflowing high-pH solution (significant consumption of Ca^{2+} and SO_4^{2-}; significant increase in Na^+, Mg^{2+} and carbonate concentrations). An alternative explanation for the similarity in solution composition between the M1 (cement zone) and M2 (fracture) sites could be given by fluid flow along a fracture where the rock matrix has already been sealed, so there is no or little diffusive exchange between fracture and matrix.

Table 7
Initial effective diffusion coefficients and constant tortuosity factors.

Domain	D_e (m^2/s), initial	τ, constant	Reference
Wall rock	3.0e-11	0.1	Steefel and Lichtner, 1998
Fracture	8.1e-10	0.9	Archie's law (exp = 2)

Fig. 3 shows mineralogy along the fracture at $t = 20$ a for the 2 cases. The largest amounts of precipitates, leading to sealing of porosity, are found near the fracture inlet. The extension of the zone of intense precipitation is larger for the reference case. Ettringite (Al end-member) fills porosity in the first 10 cm of fracture in the reference case (only about 1.5 cm in the low A's case). Significant amounts of C–S–H (Ca/Si = 1.67, close to the fracture inlet) and tobermorite and calcite (further downstream, up to about 7 m) have also precipitated in the reference case. The reference case also displays very intense dissolution of chalcedony, kaolinite, albite and dolomite in the first ca. 10 m of the fracture, together with minor dissolution of muscovite. Other phases that appear in very small amounts are mesolite, brucite and saponites. These changes in mineral contents are basically negligible (except for ettringite and some dolomite dissolution) in the case with small areas.

Fig. 4 shows mineralogy normal to the fracture next to the

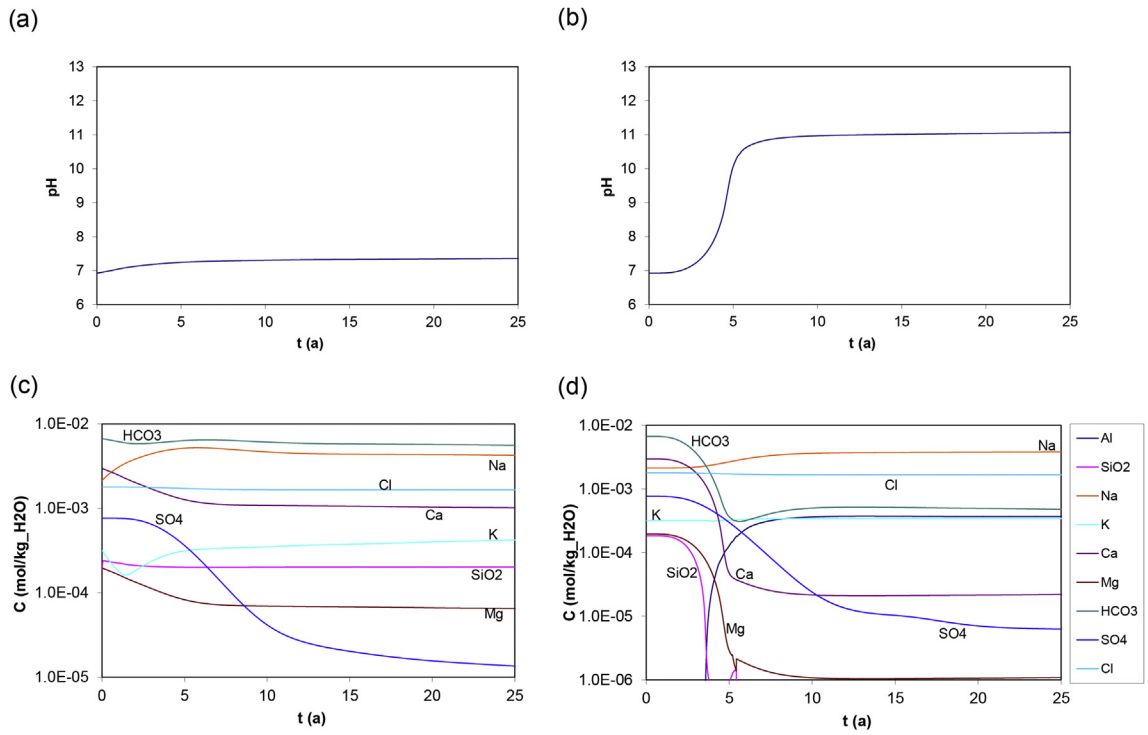

Fig. 2. Evolution of solution composition at the fracture outlet for the reference case (a,c) and the case with smaller surface areas for primary minerals (b,d).

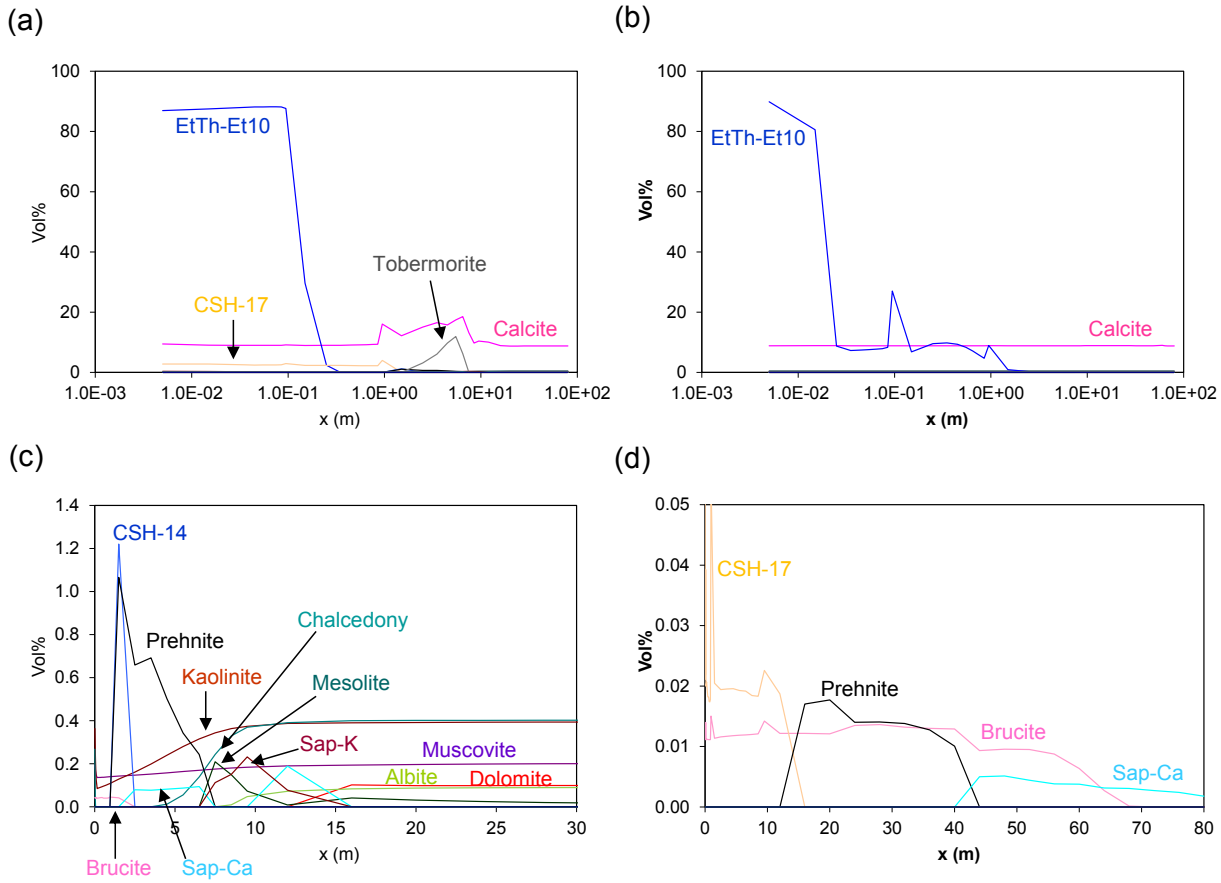

Fig. 3. Mineral contents (vol%) along the fracture at $t = 20$ a for the reference case (a,c) and the case with smaller surface areas for the primary minerals (b,d). The plots (a) and (b) have distance in logarithmic scale to show the changes very close to the fracture inlet.

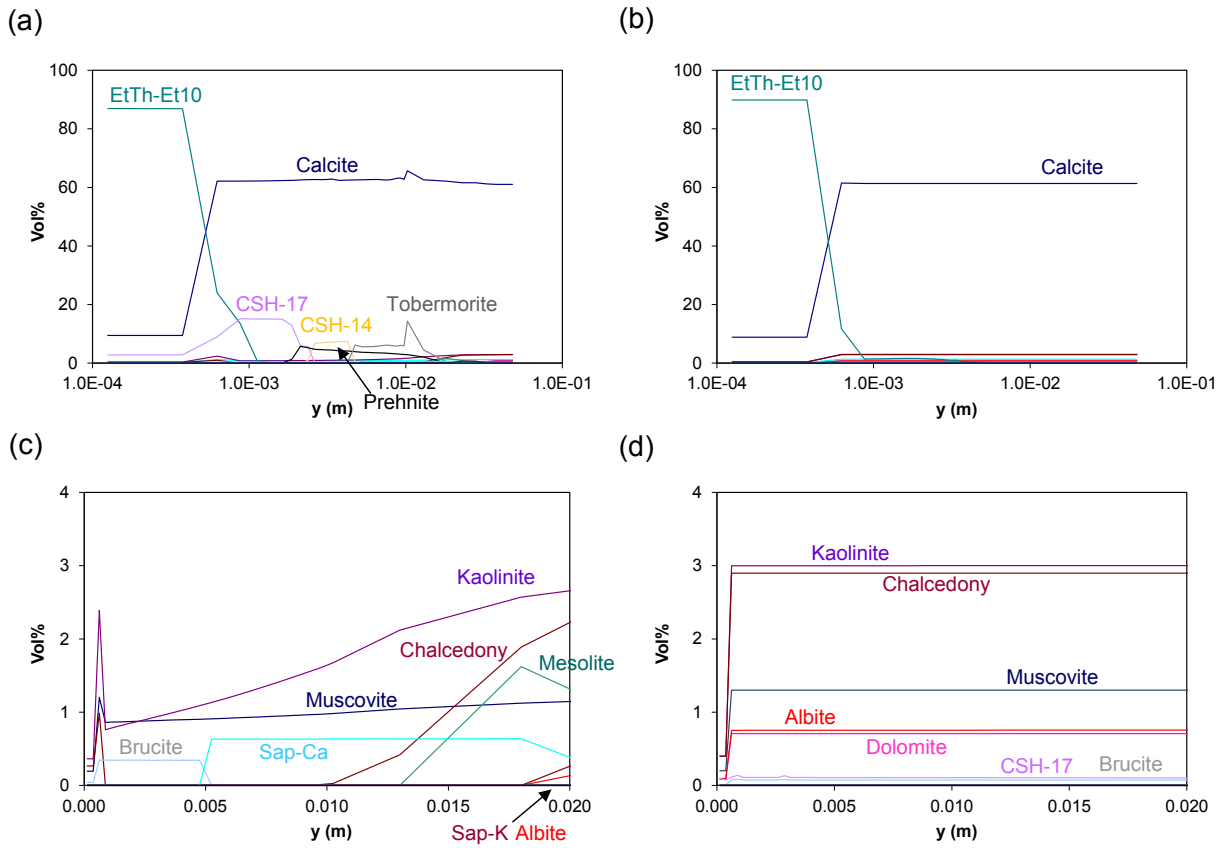

Fig. 4. Mineral contents (vol%) normal to the fracture next to the fracture inlet (x = 5e-3 m) at t = 20 a for the reference case (a,c) and the case with smaller surface areas for the primary minerals (b,d). The plots (a) and (b) have distance in logarithmic scale to show the changes very close to the fracture – wall rock interface (y = 5e-4 m).

fracture inlet (x = 5e-3 m) at t = 20 a for the 2 cases. After 20 years, mineralogy in that profile remains almost constant (very little change with respect to results after 10 a), due to sealing of porosity at the fracture. The results for the reference case show precipitation of ettringite and minor C–S–H 1.67 at the fracture and at the interface with the wall rock, followed by zones dominated gradually by C–S–H 1.67, C–S–H 1.4 and tobermorite (gradual decrease in Ca/Si ratio of the C–S–H phases), together with prehnite (C–A–S–H). There is also partial dissolution of kaolinite and chalcedony in the wall rock (supply of Si for C–S–H and C–A–S–H), and minor precipitation of brucite, saponite and mesolite. Albite and dolomite have dissolved completely in the wall rock up to about 1.5 cm from the fracture. The magnitude of mineral alteration in the wall rock in the case with small areas is much smaller.

The mineralogical alteration along the fracture (reference case) is characterized by the advance of the calcite and ettringite precipitation fronts. Besides the supply of solute by the inflowing water, calcite precipitation is controlled by the diffusion of carbonate from the wall rock, while ettringite precipitation is controlled mainly by (i) diffusion of sulfate from the wall rock and (ii) diffusion of the Al supplied by the dissolution of albite (slower dissolution in the case with smaller surface areas). The inflowing high-pH solution is at equilibrium with ettringite (Al end member) and calcite and is undersaturated with respect to the other members of the ettringite–thaumasite solid solution series.

Mineralogy in the fracture is overall consistent with observations at Maqarin (ettringite as the main fracture fill), except for the effects of fracture sealing and reactivation not included in the simulations (disturbance of the mineral zonations formed during a single fracture flow episode and leading to complex mineral textures). Similarly, mineralogy (C–S–H, C–A–S–H) and extent (ca. 2 cm) of alteration in the wall rock in the reference case are also overall consistent with observations at Maqarin, except again for the possible effect of fracture sealing and reactivation. It has to be noted that gypsum is reported as a secondary mineral at Maqarin, but it has not precipitated in any of the simulations. Gypsum formation may be related to oxidation of the small amounts of pyrite in the rock or to seasonal drying.

Fig. 5 shows porosity along the fracture (first meter) at t = 20 a for the 2 cases. Notice that fracture porosity has been clogged for the first 10 cm in the reference case, while only the very first node shows complete clogging for the small areas case. At this rate it would take about 16,000 years for the fracture to clog along the whole domain in the reference case. Fig. 6 shows porosity normal to the fracture for the 2 cases at t = 20 a and at 2 different positions along the fracture: x = 5e-3 m (fracture inlet) and x = 1.5 m. The plots show that the fracture is sealed in both cases at the inlet (x = 5e-3 m) but is not at x = 1.5 m. For the reference case there is a decrease in porosity in the wall rock within ca. 1.5 cm from the fracture, caused by a tobermorite and calcite precipitation peak (see Fig. 4), linked to dolomite dissolution. This decrease in porosity is more pronounced near the fracture inlet and is negligible in the case with small areas.

The calculated decrease in porosity is in qualitative agreement with the observed systematic decrease in porosity next to the fractures caused by C–S–H precipitation reported by Martin et al. (2014) and Martin and Leemann (2014), although in some cases the observed decrease in porosity is only partial. The instances of porosity increase next to fractures linked to carbonate dissolution

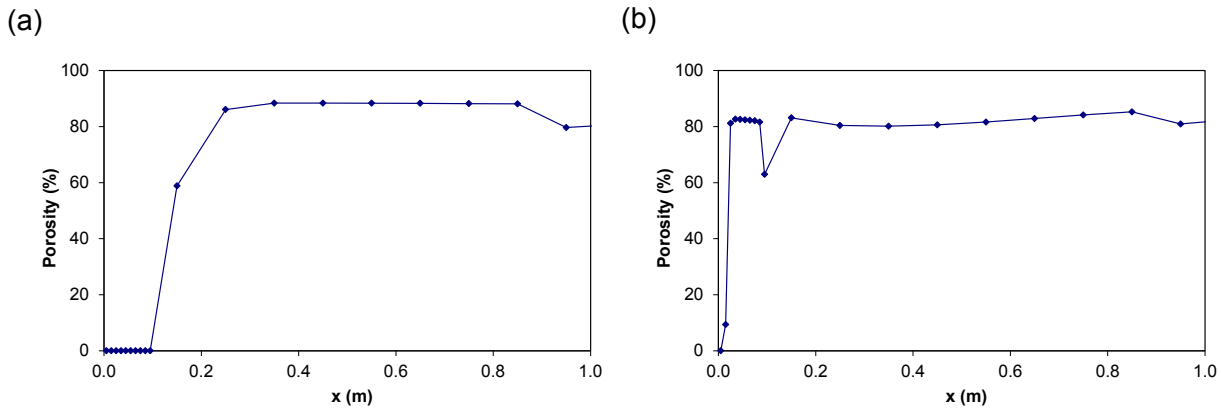

Fig. 5. Porosity (%) along the fracture at $t = 20$ a for the reference case (a) and the case with smaller surface areas for the primary minerals (b). Only the first meter is shown.

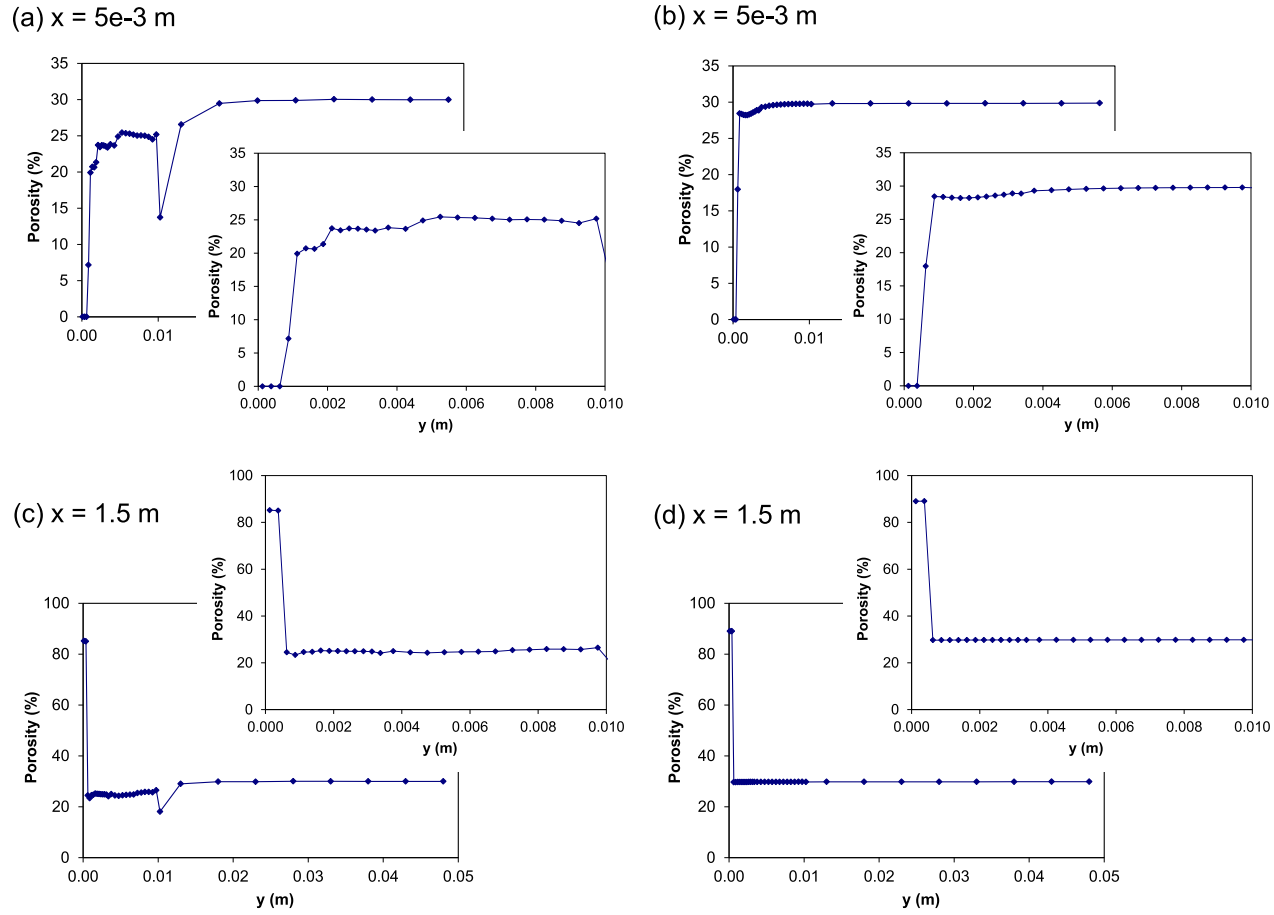

Fig. 6. Porosity (%) normal to the fracture at $t = 20$ a for the reference case (a,c) and the case with smaller surface areas for the primary minerals (b,d). Two different positions along the fracture are shown: x = 5e-3 m (fracture inlet) and x = 1.5 m. Fracture − wall rock interface is at y = 5e-4 m.

(Linklater, 1998; Smellie, 1998) are not reproduced by the model and could be related to heterogeneities in the composition of the carbonate minerals (e.g. aragonite or dolomite vs. calcite) or of the incoming high-pH solutions.

Fig. 7 shows pH along the fracture and at two different positions normal to the fracture (x = 5e-3 m and x = 44 m) for $t = 20$ a and for the two cases. Notice the small change in pH for the case with small areas, due to the much lesser amount of mineral reaction. Fig. 1S (Supporting Material) shows pH distribution in the calculation domain for the 2 cases at $t = 20$ a.

5.2. *Case with larger flow velocity in the fracture ($q = 100{,}000$ m/a)*

Measured solution composition at the M2 site is almost identical to the inflowing high-pH solution (M1 and M2 sites, Smellie, 1998). Unlike the reference case, the case with a large value of q (based on the value calculated by Steefel and Lichtner, 1998) shows a solution composition at the fracture outlet clearly evolving to a composition

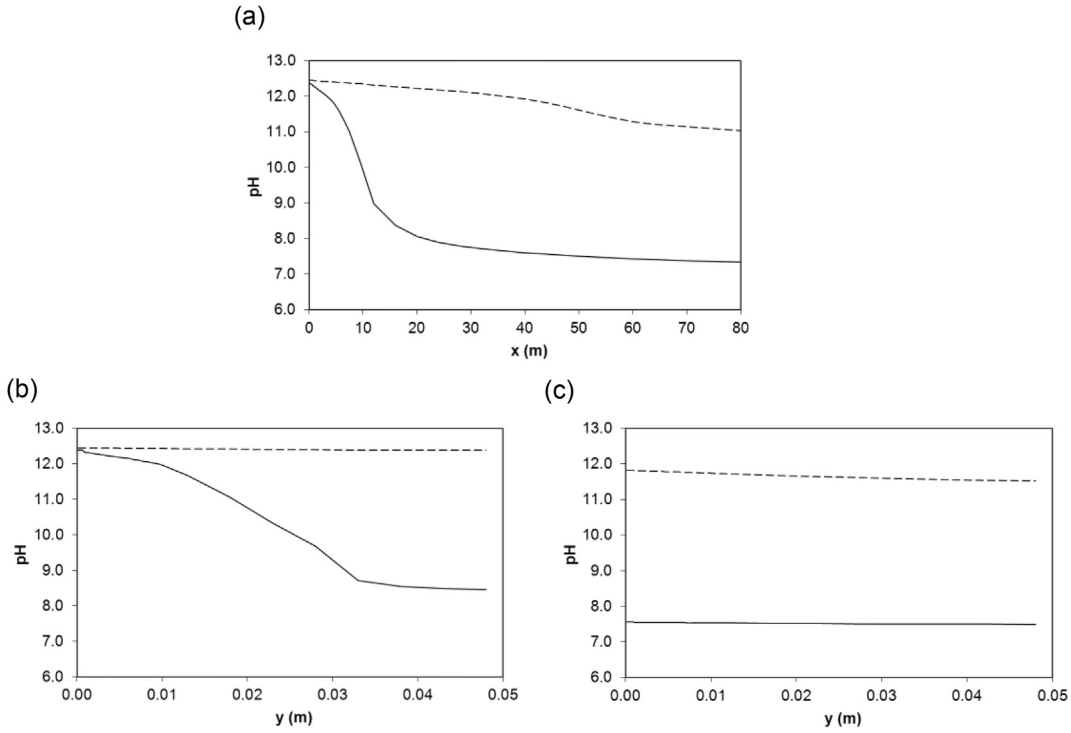

Fig. 7. pH at $t = 20$ a for the reference case (solid lines) and the case with smaller surface areas for the primary minerals (dashed lines). (a) pH along the fracture. (b) pH normal to the fracture at x = 5e-3 m (fracture inlet). (c) pH normal to the fracture at x = 44 m. Fracture − wall rock interface is at y = 5e-4 m.

similar to the inflowing high-pH solution. Fig. 2S (Supporting Material) shows the evolution of solution composition (breakthrough) at the fracture outlet. After about 0.1 a pH is almost constant, changing slowly from 12.2 to 12.5.

No porosity clogging has occurred at the fracture inlet in the case with the large q, due to the smaller amount of precipitates. There is only a minor decrease in porosity spread all along the fracture. Fig. 8 shows porosity normal to the fracture at $t = 20$ a and at 2 different positions along the fracture: x = 5e-3 m (fracture inlet) and x = 80 m (fracture outlet). The plots show that the fracture is not sealed for the case with the large q (only a minor decrease in porosity) but there is clogging of porosity in the wall rock next to the fracture, all along the fracture. This is due to the intense mineralogical alteration in the wall rock along the whole domain, caused by the almost constant composition of the solution along the fracture. In the reference case, flow was much slower and the residence time of the solution in the fracture was much longer, causing important changes in solution composition (Fig. 7).

5.3. *Case with larger sulfate concentration in the inflowing solution*

The larger sulfate concentration in the inflowing high-pH solution (see Table 3) corresponds to the value reported by Smellie (1998). Accordingly, Al concentration is about a factor of 20 smaller than in the reference case to maintain equilibrium with respect to ettringite. The objective is not to promote ettringite precipitation only by circulating a solution already supersaturated with respect to this phase. However, the solution is supersaturated with respect to the other terms of the ettringite−thaumasite solid solution series (EtTh-Et08 to EtTh-Et00). Results for the case with larger sulfate concentrations are only shown for $t = 2$ a, due to numerical convergence problems in the calculations.

Figs. 9 and 10 show porosity along and normal to the fracture at $t = 2$ a for the high-sulfate and reference cases. Unlike the reference case, there is no sealing of porosity at the fracture inlet for the case with large SO_4^{2-} concentration. However, there is sealing of porosity in the wall rock close to the wall rock−fracture interface, due to the precipitation of thaumasite (mainly EtTh-Et00 to EtTh-Et04). Thaumasite precipitation is coupled with the dissolution of calcite and chalcedony, together with the diffusion of Ca^{2+}, SO_4^{2-}, Al^{3+} and OH^- from the high-pH solution circulating in the fracture. Thaumasite (EtTh-Et02 and EtTh-Et04) also precipitates in the fracture close to the inlet.

6. Summary and conclusions

In this modeling study, high-pH solutions were injected into a fracture simulating the Maqarin natural analogue system (A-6 adit). These 2D calculations included transport by advection-dispersion-diffusion along a single fracture and diffusion in the wall rock. Solute transport was coupled to mineral dissolution and precipitation. A limited sensitivity analysis evaluated the effect of different values of primary mineral surface areas, flow velocity and sulfate concentration of the inflowing high-pH solution. The main conclusions from the study are:

- The extent of the observed mineral alteration in the wall rock (up to 3 cm; Linklater, 1998) is consistent with the large mineral surface areas used in the reference case. These areas were calculated from a grain size in the micrometer range (r = 1 μm).
- Measurements report that solution composition at the fracture outlet (M2 site) is very similar to the inflowing high-pH solution (Linklater, 1998). Results from calculations using small surface areas for the primary minerals are similar to some extent to this observation, but significant differences remain between the 2 solutions (inlet and outlet). A possible alternative explanation could call for fluid flow along matrix-sealed fractures (no interaction between fracture and wall rock).

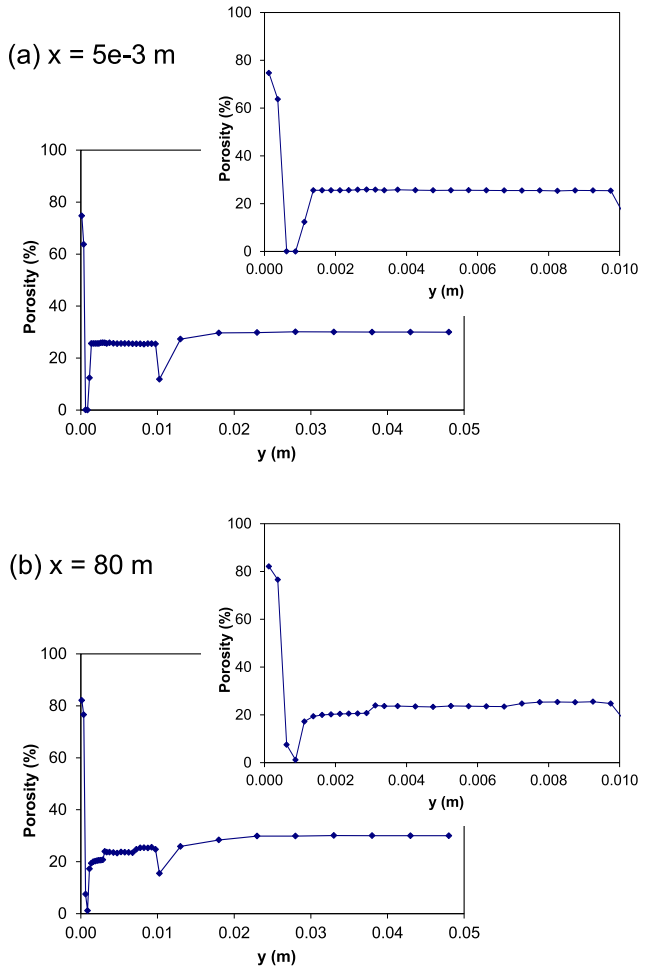

Fig. 8. Porosity (%) normal to the fracture at $t = 20$ a for the case with larger flow velocity in the fracture. Two different positions along the fracture are shown: x = 5e-3 m (fracture inlet) and x = 80 m. Fracture − wall rock interface is at y = 5e-4 m.

- Fracture sealing requires small flow velocities, but sealing is limited to the fracture inlet at the scale of tens of years. Sealing of the whole fracture would take tens of thousands of years.
- A large flow velocity in the fracture (10^5 m/a instead of 500 m/a), similar to the one used by Steefel and Lichtner (1998), causes a quasi-constant solution composition along the fracture (consistent with solution composition at the M2 site), and matrix alteration and interface sealing in the whole domain, but no (or very slow) fracture sealing. The slow decrease in porosity is spread all along the fracture. The resulting scenario shows open porosity along the fracture and sealed fracture − wall rock interface all along the domain.
- Alteration of the wall rock is limited to a zone near the fracture inlet when the smaller flow velocity is used.

Regarding mineralogy, the following observations can be made:

- The mineral responsible for the sealing of porosity in the fracture and fracture − wall rock interface is ettringite (Al end member), except in the case with large SO_4 concentration (thaumasite). Ettringite and thaumasite have been reported as the major fracture fills at the site. Ettringite precipitation is controlled by (i) the diffusion of sulfate from the wall rock (the inflowing high-pH solution is at equilibrium with respect to ettringite), and (ii) the diffusion of Al supplied by the dissolution of albite.
- Besides ettringite, significant amounts of C−S−H solid solution (Ca/Si = 1.67, close to the fracture inlet) and tobermorite and calcite (further downstream) also precipitate along the fracture in the calculations. The reference case also displays very intense dissolution of chalcedony, kaolinite, albite and dolomite in the first ca. 10 m of the fracture, together with minor dissolution of muscovite. Other phases that appear in very small amounts are mesolite, brucite and saponites.
- Normal to the fracture, the results for the reference case show precipitation of ettringite and minor C−S−H 1.67 at the fracture and at the interface with the wall rock, followed by zones dominated gradually by C−S−H 1.67, C−S−H 1.4 and tobermorite (gradual decrease in Ca/Si ratio of the C−S−H phases), together with prehnite (C−A−S−H). There is also partial dissolution of kaolinite and chalcedony in the wall rock, and minor precipitation of brucite, saponite and mesolite. The precipitation of C−S−H and C−A−S−H is responsible for the decrease in porosity in the wall rock in the calculations and is in agreement with the observations by Martin et al. (2014) and Martin and Leemann (2014). The instances of porosity increase next to fractures linked to carbonate dissolution (Linklater, 1998; Smellie, 1998) are not reproduced by the model and could be related to heterogeneities in the composition of the carbonate minerals or of the high-pH solutions. The magnitude of mineral alteration in the wall rock in the low A's case is much smaller.
- A larger sulfate concentration in the inflowing high-pH solution (Smellie, 1998) favors thaumasite precipitation but causes a

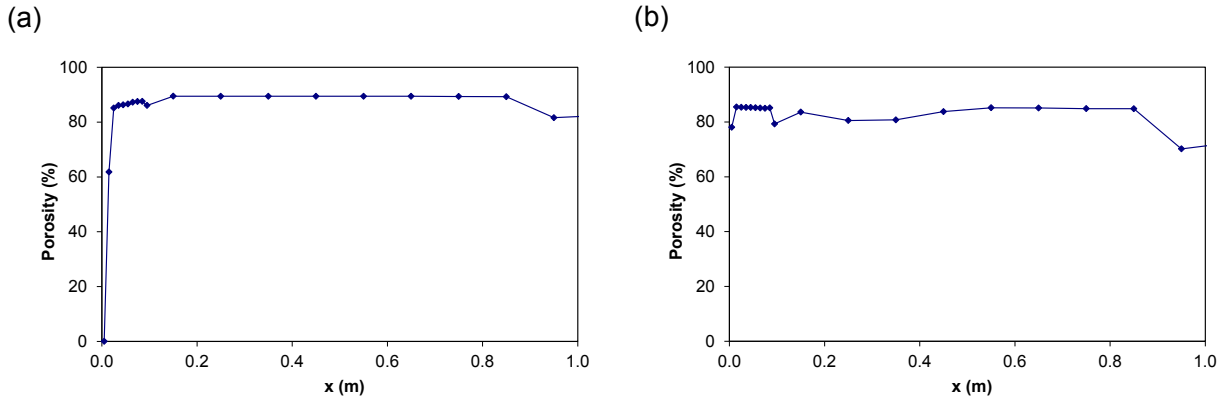

Fig. 9. Porosity (%) along the fracture at $t = 2$ a for the reference case (a) and the case with larger sulfate concentration of the high-pH solution (b). Only the first meter is shown.

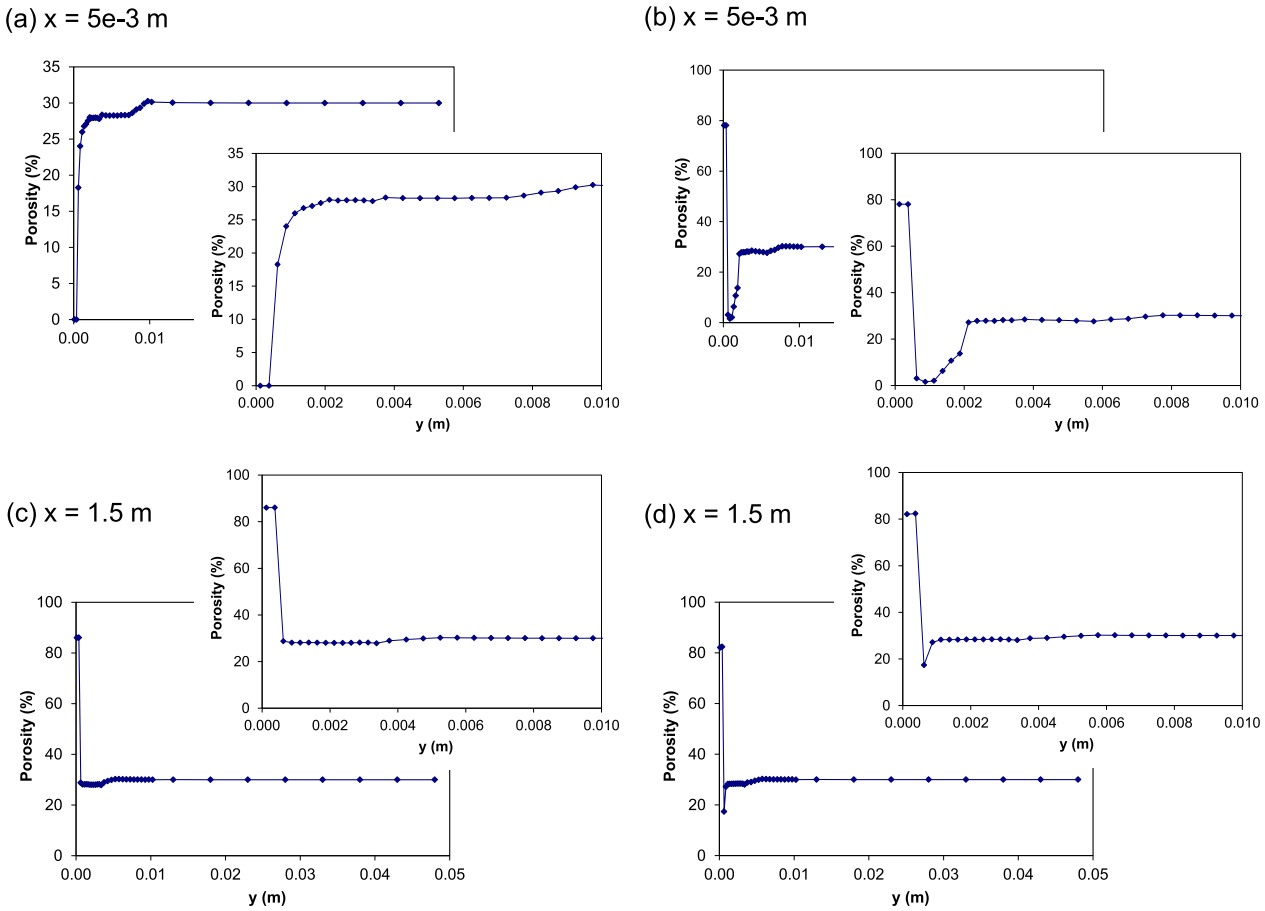

Fig. 10. Porosity (%) normal to the fracture at $t = 2$ a for the reference case (a,c) and the case with larger sulfate concentration of the high-pH solution (b,d). Two different positions along the fracture are shown: x = 5e-3 m (fracture inlet) and x = 1.5 m. Fracture – wall rock interface is at y = 5e-4 m.

much slower reduction of porosity in the fracture. However, the fracture – wall rock interface is sealed very quickly. Thaumasite precipitation at this interface is coupled to the dissolution of calcite and chalcedony, together with the diffusion of Ca, SO_4, Al and OH^- from the high-pH solution circulating in the fracture.

It should be noted that flow velocity was assumed to be constant in the fracture, despite changes or even the complete sealing of fracture porosity. This is certainly a simplification which does not take into account the complex 2D/3D and time-dependent nature of flow in the fracture. The fracture sealing and reactivation evidenced in the mineralogy and structure of the fracture infills at Maqarin were not included in the simulations.

Besides the evident effect of fracture sealing and reactivation in the structure and mineralogy of alteration, it should be noted that a single high-pH fluid composition can explain the ettringite-dominated fracture fillings and the decrease in porosity caused by C–S–H and C–A–S–H in the wall rock next to the fractures. Silicate and aluminosilicate dissolution (chalcedony, kaolinite) provide the silica for C–S–H and C–A–S–H without the need for calling for different types of solutions.

Acknowledgments

The GTS-LCS project is financed by the following agencies: Japan Atomic Energy Agency, Nationale Genossenschaft für die Lagerung radioaktiver Abfälle (Switzerland), Radioactive Waste Management (UK), Posiva Oy (Finland) and Svensk Kärnbränslehantering AB (Sweden). The funding for this modeling study from Posiva Oy and the discussions with the numerous members of the GTS-LCS team (JAEA, NAGRA, RWM, POSIVA, SKB, University of Bern, Eidgenössische Materialprüfungs und Forschungsanstalt – Switzerland, Paul Scherrer Institut – Switzerland, UFZ Leipzig – Germany, Quintessa – UK, Savage Earth – UK, Obayashi – Japan, Vattenfall – Sweden), are gratefully acknowledged. The comments and suggestions by three anonymous reviewers and by the journal editor, Prof. Michael Kersten, contributed very positively to the final version of the manuscript.

Appendix A. Supplementary data

Supplementary data related to this article can be found at http://dx.doi.org/10.1016/j.apgeochem.2015.12.012.

References

Adler, M., 2001. Interaction of Claystone and Hyperalkaline Solutions at 30°C: a Combined Experimental and Modeling Study. PhD Dissertation. Univ. Bern.

Alexander, W.R., Dayal, R., Eagleson, K., Eikenberg, J., Hamilton, E., Linklater, C.M., McKinley, I.G., Tweed, C.J., 1992. A natural analogue of high pH cement pore waters from the Maqarin area of northern Jordan. II: results of predictive geochemical calculations. J. Geochem. Explor 46, 133–146.

Baker, A.J., Bateman, K., Hyslop, E.K., Ilett, D.J., Linklater, C.M., Milodowski, A.E., Noy, D.J., Rochelle, C.A., Tweed, C.J., 2002. Research on the Alkaline Disturbed Zone Resulting from Cement-water-rock Reactions Around a Cementitious Repository. Nirex Report N/054, Harwell, UK.

Bandstra, J.Z., Buss, H.L., Campen, R.K., Liermann, L.J., Moore, J., Hausrath, E.M.,

Navarre-Sitchler, A.K., Jang, J.-H., Brantley, S.L., 2008. Appendix: compilation of mineral dissolution rates. In: Brantley, S.L., Kubicki, J.D., White, A.F. (Eds.), Kinetics of Water-rock Interaction. Springer.
Burch, T.E., Nagy, K.L., Lasaga, A.C., 1993. Free energy dependence of albite dissolution kinetics at 80 °C and pH 8.8. Chem. Geol. 105, 137–162.
Carey, J.W., Lichtner, P.C., 2006. Calcium Silicate Hydrate Solid Solution Model Applied to Cement Degradation Using the Continuum Reactive Transport Model FLOTRAN. Report LA-UR-06-0636. Los Alamos National Laboratory, Los Alamos.
Carey, J.W., Lichtner, P.C., 2007. Calcium silicate hydrate (C-S-H) solid solution model applied to cement degradation using the continuum reactive transport model FLOTRAN. In: Mobasher, B., Skalny, J. (Eds.), Transport Properties and Concrete Quality: Materials Science of Concrete, Special Volume. American Ceramic Society, pp. 73–106.
Chambers, A.V., Haworth, A., 1998. Coupled modelling for the Jordan natural analogue project. In: Linklater, C.M. (Ed.), (1998) a Natural Analogue Study of Cement-buffered, Hyperalkaline Groundwaters and Their Interaction with a Repository Host Rock. Phase II. Nirex Report No. S/98/003, Harwell, UK.
Clark, I.D., Fritz, P., Seidlitz, H.K., Trimborn, P., Milodowski, T.E., Pearce, J.M., Khoury, H.N., 1993. Recarbonation of metamorphosed marls. Jordan. Appl. Geochem 8, 473–481.
Clark, I.D., Khoury, H.N., Salameh, E., Fritz, P., Seidlitz, H.K., Milodowski, T.E., 1992. Origin of the Maqarin, Jordan hyperalkaline groundwaters: isotopic and geochemical evidence for in situ combustion, calcination and recarbonation of bituminous marls. In: Proceedings of the 7th International Symposium on Water-rock Interaction. Balkema, Rotterdam, pp. 1485–1489.
Edge, R.A., Taylor, H.F.W., 1971. Crystal structure of thaumasite, $[Ca_3Si(OH)_6.12H_2O](SO_4)(CO_3$. Acta Cryst. B27, 594–601.
Gaucher, E.C., Blanc, Ph, Matray, J.-M., Michau, N., 2004. Modeling diffusion of an alkaline plume in a clay barrier. Appl. Geochem 19, 1505–1515.
Hoch, A.R., Linklater, C.M., Noy, D.J., Rodwell, W.R., 2004. Modelling the interaction of hyperalkaline fluids with simplified rock mineral assemblages. Appl. Geochem 19, 1431–1451.
Honty, M., De Craen, M., Wang, L., Madejová, J., Pentrák, M., Strícek, I., Van Geet, M., 2010. The effect of high pH alkaline solutions on the mineral stability of the boom clay – batch experiments at 60 °C. Appl. Geochem 25, 825–840.
Hummel, W., Berner, U., Curti, E., Pearson, F.J., Thoenen, T., 2002. Nagra/PSI Chemical Thermodynamic Data Base 01/01. Nagra Technical Report 02–16, Wettingen, Switzerland.
Khoury, H.N., 1985. The origin of highly alkaline waters from the Maqarin area, north Jordan. Dirasat Sci. Geogr.) 12, 125–131.
Khoury, H.N., Milodowski, T.E., 1992. High temperature metamorphism and low temperature retrograde alteration of spontaneously combusted marls: the Maqarin cement analogue, Jordan. In: Proceedings of the 7th International Symposium on Water-rock Interaction. Balkema, Rotterdam, pp. 1515–1518.
Khoury, H.N., Salameh, E., 1985. Leaching of Ruseifa phosphates and Maqarin bituminous limestome and its effect on the quality of groundwater. Dirasat Sci. Geogr.) 12, 81–98.
Khoury, H.N., Salameh, E., Abdul-Jaber, Q., 1985. Characteristics of an unusual highly alkaline water from the Maqarin area, Northern Jordan. J. Hydrol. 81, 79–91.
Khoury, H.N., Salameh, E., Clark, I.D., Fritz, P., Bajjali, W., Milodowski, A.E., Cave, M.R., Alexander, W.R., 1992. A natural analogue of high pH cement pore waters from the Maqarin area of northern Jordan. I: introduction to the site. J. Geochem. Explor 46, 117–132.
Kosakowski, G., Berner, U., 2013. The evolution of clay rock/cement interfaces in a cementitious repository for low- and intermediate level radioactive waste. Phys. Chem. Earth 64, 65–86.
Kulik, D.A., Kersten, M., 2001. Aqueous solubility diagrams for cementitious waste stabilization systems: II, end-member stoichiometries of ideal calcium silicate hydrate solid solutions. J. Am. Ceram. Soc. 84, 3017–3026.
Lichtner, P.C., Carey, J.W., 2006. Incorporating solid solutions in reactive transport equations using a kinetic discrete-composition approach. Geochim. Cosmochim. Acta 70, 1356–1378.
Linklater, C.M. (Ed.), 1998. A Natural Analogue Study of Cement-buffered, Hyperalkaline Groundwaters and Their Interaction with a Repository Host Rock. Phase II. Nirex Report No. S/98/003, Harwell, UK.
Linklater, C.M., Albinsson, Y., Alexander, W.R., Casas, I., McKinley, I.G., Sellin, P., 1996. A natural analogue of high-pH cement pore waters frm the Maqarin area of northern Jordan: comparison of predicted and observed trace-element chemistry of uranium and selenium. J. Contam. Hydrol. 21, 56–69.
Mäder, U.K., Th, Fierz, Frieg, B., Eikenberg, J., Rüthi, M., Albinsson, Y., Möri, A., Ekberg, S., 2005. Interaction of hyperalkaline fluid with fractured rock: field and laboratory experiments of the HPF project (Grimsel test Site, Switzerland). J. Geochem. Explor 90, 68–94.
Martin, L., Leemann, A., 2014. Maqarin (Jordan) – a Natural Cement Analog Study. Phase Characterization on Four Selected Samples. Nagra Arbeitsbericht NAB, Wettingen, Switzerland, pp. 13–90.
Martin, L.H.J., Leemann, A., Mäder, U.K., Rüedi, J., 2014. Secondary mineral formation and porosity changes in the proximity of a natural cement analog (Maqarin, Jordan). In: Conference Proceedings, NUWCEM 2014 – 2nd International Symposium on Cement-based Materials for Nuclear Wastes.
Marty, N.C.M., Munier, I., Gaucher, E.C., Tournasat, C., Gaboreau, S., Vong, C.Q., Giffaut, E., Cochepin, B., Claret, F., 2014. Simulation of cement/clay interactions: feedback on the increasing complexity of modeling strategies. Transp. Porous Media 104, 385–405.
Marty, N.C.M., Tournassat, C., Burnol, A., Giffaut, E., Gaucher, E.C., 2009. Influence of reaction kinetics and mesh refinement on the numerical modelling of concrete/clay interactions. J. Hydrol. 364, 58–72.
Morse, J.W., Arvidson, R.S., 2002. The dissolution kinetics of major sedimentary carbonate minerals. Earth Sci. Rev. 58, 51–84.
Moyce, E.B.A., Rochelle, C., Morris, K., Milodowski, A.E., Chen, X., Thornton, S., Small, J.S., Shaw, S., 2014. Rock alteration in alkaline cement waters over 15 years and its relevance to the geological disposal of nuclear waste. Appl. Geochem 50, 91–105.
Palandri, J.L., Kharaka, Y.K., 2004. A Compilation of Rate Parameters of Water-Mineral Interaction Kinetics for Application to Geochemical Modeling. U.S. Geological Survey, Menlo Park, USA. Open File Report 2004-1068.
Pitty, A.F., Alexander, W.R. (Eds.), 2011. A Natural Analogue Study of Cement Buffered, Hyperalkaline Groundwaters and Their Interaction with a Repository Host Rock IV: an Examination of the Khushaym Matruk (Central Jordan) and Maqarin (Northern Jordan) Sites. Bedrock Geosciences Technical Report 11–02, Auenstein, Switzerland.
Read, D., Glasser, F.P., Ayora, C., Guardiola, M.T., Sneyers, A., 2001. Mineralogical and microstructural changes accompanying the interaction of boom clay with ordinary Portland cement. Adv. Cem. Res. 13, 175–183.
Sánchez, L., Cuevas, J., Ramírez, S., Riuiz De León, D., Fernández, R., Vigil Dela Villa, R., Leguey, S., 2006. Reaction kinetics of FEBEX bentonite in hyperalkaline conditions resembling the cement-bentonite interface. Appl. Clay Sci. 33, 125–141.
Savage, D., Noy, D., Mihara, M., 2002. Modelling the interaction of bentonite with hyperalkaline fluids. Appl. Geochem 17, 207–223.
Savage, D., Soler, J.M., Yamaguchi, K., Walker, C., Honda, A., Inagaki, M., Watson, C., Wilson, J., Benbow, S., Gaus, I., Rueedi, J., 2011. A comparative study of the modelling of cement hydration and cement-rock laboratory experiments. Appl. Geochem 26, 1138–1152.
Schmidt, T., Lothenbach, B., Romer, M., Scrivener, K., Rentsch, D., Figi, R., 2008. A thermodynamic and experimental study of the conditions of thaumasite formation. Cem. Concr. Res. 38, 337–349.
Shao, H., Kosakowski, G., Berner, U., Kulik, D.A., Mäder, U., Kolditz, O., 2013. Reactive transport modeling of the clogging process at Maqarin natural analogue site. Phys. Chem. Earth 64, 21–31.
Smellie, J.A.T. (Ed.), 1998. Maqarin Analogue Study: Phase III. SKB Technical Report TR-98-04, Stockholm, Sweden.
Soler, J.M., 2003. Reactive transport modeling of the interaction between a high-pH plume and a fractured marl: the case of Wellenberg. Appl. Geochem 18, 1555–1571.
Soler, J.M., 2013. Reactive transport modeling of concrete-clay interaction during 15 years at the Tournemire underground rock laboratory. Eur. J. Mineral. 25, 639–654.
Soler, J.M., Lasaga, A.C., 1996. A mass transfer model of bauxite formation. Geochim. Cosmochim. Acta 24, 4913–4931.
Soler, J.M., Mäder, U.K., 2005. Interaction between hyperalkaline fluids and rocks hosting repositories for radioactive waste: reactive transport simulations. Nucl. Sci. Eng. 151, 128–133.
Soler, J.M., Mäder, U.K., 2007. Mineralogical alteration and associated permeability changes induced by a high-pH plume: modeling of a granite core infiltration experiment. Appl. Geochem 22, 17–29.
Soler, J.M., Mäder, U.K., 2010. Cement-rock interaction: infiltration of a high-pH solution into a fractured granite core. Geol. Acta 8, 221–233.
Soler, J.M., Vuorio, M., Hautojärvi, A., 2011. Reactive transport modeling of the interaction between water and a cementitious grout in a fractured rock. Application to ONKALO (Finland). Appl. Geochem 26, 1115–1129.
Steefel, C.I., 2009. CrunchFlow. Software for Modeling Multicomponent Reactive Flow and Transport. User's Manual. Lawrence Berkeley National Laboratory, Berkeley.
Steefel, C.I., Appelo, C.A.J., Arora, B., Jacques, D., Kalbacher, T., Kolditz, O., Lagneau, V., Lichtner, P.C., Mayer, K.U., Meeussen, J.C.L., Molins, S., Moulton, D., Shao, H., Simunek, J., Spycher, N., Yabusaki, S.B., Yeh, G.T., 2015. Reactive transport codes for subsurface environmental simulation. Comput. Geosci. 19, 445–478.
Steefel, C.I., Lichtner, P.C., 1998. Multicomponent reactive transport in discrete fractures II: infiltration of hyperalkaline groundwater at Maqarin, Jordan, a natural analogue site. J. Hydrol. 209, 200–224.
Taylor, H.F.W., 1997. Cement Chemistry, second ed. Thomas Telford, London.
Wolery, T.J., Jackson, K.J., Bourcier, W.L., Bruton, C.J., Viani, B.E., Knauss, K.G., Delany, J.M., 1990. Current status of the EQ3/6 software package for geochemical modeling. In: Melchior, C., Bassett, R.L. (Eds.), Chemical Modeling of Aqueous Systems II, ACS Symposium Series No 416, pp. 104–116.